DOI: 10.1002/((please add manuscript number))
Article type: Communication

Constructing Hierarchically Hollow Core-Shell MnO_2/C Hybrid Spheres for High-Performance Lithium Storage

Gang Wang, Yuhan Sun, Debao Li, Wei Wei, Xinliang Feng and Klaus Müllen**

G. Wang, Prof. Y. Sun, Prof. D. Li
State Key Laboratory of Coal Conversion, Institute of Coal Chemistry, Chinese Academy of Sciences, 030001 Taiyuan, China
G. Wang, Dr. Wei Wei, Prof. K. Müllen
Max Planck Institute for Polymer Research, Achermannweg 10, 55128 Mainz, Germany
E-mail: muellen@mpip-mainz.mpg.de
Prof. X. Feng
Center for Advancing Electronics Dresden (cfaed) & Department of Chemistry and Food Chemistry, Technische Universität Dresden, 01062 Dresden, Germany
E-mail: xinliang.feng@tu-dresden.de
G. Wang
University of Chinese Academy of Sciences, 100049 Beijing, China

Keywords: hierarchical structures, hollow core-shell, mesoporous MnO_2, hybrids, Li-ion batteries

Lithium ion batteries (LIBs) with higher energy density and longer cycling life have been widely explored to meet the ever-growing energy storage demands for portable electronic devices, electric transportation system and even grid applications.[1] As a crucial component, electrode material plays a vital role in pursuing high-performance LIBs. To replace the commercial graphite anode which has a limited theoretical capacity of 372 mAh g^{-1}, extensive efforts have been devoted to developing electrochemically active materials with high reversible capacity, such as Si,[2] Ge,[3] Sn[4] and transition metal oxides[5]. Among these materials, MnO_2 is considered as a promising anode candidate due to its natural abundance, environmental friendliness, cost effectiveness and high theoretical capacity up to 1232 mAh g^{-1}.[6] The main challenges associated with MnO_2 anodes are low electrical conductivity and significant volume variation during the lithiation and delithiation cycles, which lead to

instable solid-electrolyte interphase (SEI) and mechanical failure of electrode, therefore, resulting into poor cycling stability and rate capability.

By far three effective strategies have been proposed to address the above drawbacks and improve the electrochemical performance of large-volume-change lithium battery anodes. The first strategy is binding MnO_2 with various conductive hosts (carbon nanotubes,[6a, 6c, 7] graphene,[6d, 6f, 8] Ni foam,[9] etc.) to boost the electrical conductivity and alleviate structural degradation of MnO_2 electrodes (**Scheme 1**a). However, the MnO_2 that is weakly attached to the surface of conductive materials may aggregate and detach during the repeated expansion-contraction cycles, finally lose the electrical contact, leading to continuous capacity fading. The second strategy is the fabrication of yolk-shell structures (Si@C,[10] Fe_2O_3@C,[11] Mn_3O_4@C[12] and S@PANi[13]) to confine the volume change of active materials within the hollow conductive shells, eventually enhancing the mechanical stability of electrodes (Scheme 1b). However, the contact mode of active material with the conductive shell (point-to-point or line-to-line) may retard the fast transport of both electrons and lithium ions from/to the active materials and make the contact ineffective.[14] The third strategy is to construct hollow core-shell structures with well-defined inner voids and a perfect face-to-face contact mode (Scheme 1c). In this respect, the inner voids can provide free space for volume change of active materials and fast Li ions transport, while the face-to-face contact mode guarantees a reliable electrical connection. Even though hollow core-shell structures (Si@Ag[15] and Si@PPy spheres[16]) have been proposed for high-performance Si anodes, such a unique design has seldom been reported in transition metal oxide anodes, partially because it is challenging to achieve uniform hollow metal oxide nanostructures.

In this work, a novel hierarchically hollow core-shell MnO_2/C superstructure has been constructed and evaluated as the anode of LIBs. Mesoporous carbon spheres (MCSs, **Figure 1**a), consisting of numerous interconnected hollow carbon nanospheres, act as open porous

framework for directional growth of MnO_2 onto the inner surface of carbon shell, generating the hierarchically hollow core-shell MnO_2/C hybrid spheres (MCS@MnO_2, Figure 1a). The presence of well-defined inner voids and continuous carbon framework in such architecture can effectively solve the volume variation and conductive problems that are associated with MnO_2 anodes. On the other hand, the MCS@MnO_2 can be regarded as secondary particles assembled from primary hollow core-shell MnO_2@C nanospheres. The close packing of MnO_2@C building blocks in MCS@MnO_2 will ensure a high tap density of our nanostructured material, affording both high gravimetric and volumetric capacities. When serving as LIB anodes, the hierarchical MnO_2/C hybrid spheres with high MnO_2 loading (60-90%) exhibited excellent electrochemical performance including large specific capacity (1000-1100 mAh g^{-1} at 0.1 A g^{-1}), superior rate capability and long-term cycling stability. Notably, a volumetric capacity up to 1200 mAh cm^{-3} was achieved, which is among the highest values of all reported MnO_2 anodes and even comparable to state-of-the-art Si nanostructured electrodes.[10b, 17]

As illustrated in Figure 1a, the synthetic procedure leading to hierarchical MnO_2/C hybrid spheres comprises two consecutive steps: preparation of MCSs and directional growth of MnO_2 on the pore walls of MCSs. First, uniform SiO_2@polyaniline (PANI) composite spheres were fabricated via co-assembly of colloidal silica nanoparticles with PANI.[18] After carbonization and removal of sacrificial SiO_2 template, MCSs featuring well-defined open pores, high surface area and large pore volume (Figure S1, S2 and Table S1) were prepared. In contrast to other carbon materials that possess outer surface (carbon fiber and solid carbon sphere)[19] or both outer/inner surface (hollow carbon sphere, carbon nanotube and CMK-5)[6a, 20], our MCSs mainly expose inner concave surface of hollow carbon nanospheres (Figure 1c), which can serve as ideal carbon substrate to construct hollow core-shell structures. Second, the directional deposition of MnO_2 onto the pore walls of MCSs was conducted by reacting

surface carbon layer of MCSs with $KMnO_4$ at room temperature via reaction: 4 $KMnO_4$+3 C+H_2O→4 MnO_2+K_2CO_3+2 $KHCO_3$. The loading content of MnO_2 can be readily modulated by modifying the reaction parameters such as reaction time and $KMnO_4$ concentration. The effective exposure of MCSs' inner concave surface together with controlled deposition of MnO_2 onto the pore walls of MCSs finally generate hierarchically hollow core-shell MnO_2/C hybrid spheres (MCS@MnO_2). For clarity, MCS@MnO_2-*x* refers to sample prepared by reacting MCSs with $KMnO_4$ for *x* h. The fabrication details are summarized in the Supporting Information (SI).

Polymerization of aniline in presence of colloidal silica produced uniform SiO_2@PANI composite spheres, as demonstrated by the scanning electron microscope (SEM) image in Figure 1b. The SiO_2 nanoparticles (~22 nm) were homogeneously embedded into the PANI matrix. After carbonization and etching treatment, monodisperse MCSs with particle size of around 200 nm and a unique spherical morphology were achieved; and well-defined mesopores were developed throughout the carbon spheres (Figure 1c and S1). The porous features of MCSs were then inspected by N_2 adsorption-desorption measurements (Figure S2). The isotherms of MCSs exhibited type–IV isotherm characteristics as well as a steep capillary condensation step in P/P_0 range of 0.85-0.95, which indicates the uniform generation of extra-large mesopores. A large H2-type hysteresis loop with delayed capillary evaporation was observed at P/P_0 of ~0.5, implying caged mesopores with small windows on the pore walls.[21] The pore size distribution curve further revealed that the small windows were <2 nm in dimension (Figure S2b). These results suggest a continuous porous structure of MCSs constructed from ultrathin pore walls (2-3 nm). The Brunauer-Emmett-Teller (BET) surface area of MCSs is ~900 m^2 g^{-1} together with a large pore volume of 2 cm^3 g^{-1}, making the high loading of MnO_2 onto MCSs possible.

After MnO_2 deposition, the product morphology and particle size were analogous to those of MCSs (Figure 1d and S3). By prolonging the reaction time from 2 to 24 h, the wall of MCS@MnO_2 turned thicker and the mesopores gradually shrank (Figure 1e-g), which means that more MnO_2 was loaded onto pore walls and partially occupied the inner voids of MCSs. In order to gain further insight into the change of mesopores during MnO_2 deposition, transmission electron microscopy (TEM) images under both bright and dark field were collected. As revealed in **Figure 2**a and b, MCS@MnO_2 retained the spherical morphology of MCSs and the mesopore size evolved from ~22 nm for MCSs to ~18 nm for MCS@MnO_2-2. The high resolution transmission electron microscopy (HRTEM) image in Figure 2c showed a 0.24 nm lattice spacing of the (006) planes of birnessite MnO_2.[22] Regarding MCS@MnO_2 hybrids with more MnO_2 deposited, however, the formed thick MnO_2 would make it gradually difficult to distinguish the pore size from TEM image, as shown in Figure 2d for MCS@MnO_2-24. Here ultramicrotomy, which is a common method for cutting samples into extremely thin slices that can be studied by TEM, was applied to reveal the real inner structure of MCS@MnO_2 (see SI for more details). As displayed in Figure 2e and S4, perfect round mesopores were found uniformly distributed in the ultrathin MCS@MnO_2-24 slices (~60 nm) and the pore size varied in the range of 8-12 nm. This result suggests that the MnO_2 was successfully anchored onto the inner surface of MCSs to produce hierarchically hollow core-shell MCS@MnO_2. Furthermore, the energy dispersive spectroscopic (EDS) elemental mapping images (Figure 2f) of the resultant MCS@MnO_2-24 slice provided clear evidence of the co-existence of Mn, O and C elements.

X-ray photoelectron spectroscopy (XPS) was performed to qualitatively analyze the oxidation state of Mn in the MCS@MnO_2 hybrids (Figure S5). Two strong peaks centered at 642.2 and 653.9 eV are attributed to Mn $2p_{3/2}$ and Mn $2p_{1/2}$ in MnO_2.[6c, 6f] The Raman spectra of MCS@MnO_2 in Figure S6a showed four characteristic peaks centered at 567, 633, 1348 and 1591 cm^{-1}. The former two peaks can be assigned to Mn-O lattice vibrations, while the

latter two belong to the D and G bands of graphitic carbon.[19c] The signals from C gradually faded in MCS@MnO_2 with longer reaction time, which is indicative of carbon depletion in reaction. The X-ray diffraction (XRD) patterns of MCS@MnO_2 (Figure S6b) with four peaks at 12°, 24°, 37° and 66° can be indexed to a layered birnessite-type MnO_2 (JCPDS 42-1317).[23] The porosity of MCS@MnO_2 products was further revealed by the Brunauer-Emmett-Teller (BET) analysis (Figure S6c). The surface area and pore volume of MCS@MnO_2 ranged from 142 to 30 m^2 g^{-1} and from 0.31 to 0.06 cm^3 g^{-1} (Table S1), respectively. The corresponding pore size gradually decreased from ~22 nm for MCSs to ~10 nm for MCS@MnO_2-24 (Figure S6d), which is consistent with the TEM results. The content of MnO_2 in MCS@MnO_2 samples, determined by thermalgravimetric analysis (TGA), varied from 50 to 90% (Figure S7).

The electrochemical performances of MCS@MnO_2 anodes were first evaluated by cyclic voltammetry (CV) at a scanning rate of 0.5 mV/s (**Figure 3**a). A broad peak at 0.76 V and a strong peak at low potential in the first discharge scan can be assigned to the formation of SEI and reduction of manganese dioxide to metallic manganese (Mn^{4+} to Mn^0), respectively. During the first charge process, two distinct anodic peaks were revealed at 1.2 and 2.1 V, which could be ascribed to the two-step electrochemical oxidation of manganese.[6f, 9] After activation in the first cycles, the well-overlapped peaks on the subsequent CV curves indicate an excellent cycling performance of the MCS@MnO_2 anodes. The first three discharge-charge profiles of MCS@MnO_2 anode in the potential range of 0.01-3 V vs Li/Li^+ are shown in Figure 3b. A dominant potential plateau at 0.4 V in discharge process and two potential plateaus at around 1.3 and 2.1 V in charge process match well with typical characteristics of MnO_2 anodes.[6c, 6d] The initial discharge and charge capacity of MCS@MnO_2-5 are 1480 and 1030 mAh g^{-1}, respectively, yielding an initial Coulombic efficiency (CE) of 70%. The irreversible capacity can be attributed to the formation of a SEI on the electrode surface and Li^+ trapped in amorphous carbon. [10b, 24]

The cycling performance of MCS@MnO_2 anodes was investigated by galvanostatic charge/discharge measurements within a cutoff voltage window of 0.01-3 V (Figure 3c). For comparison, the performances of control samples MCS-MnO_2-outer (MnO_2 grown on the outer periphery rather than in the mesopores of MCSs, see Figure S9) and pure MCSs were collected under the same condition. Unless otherwise noted, all the specific capacities reported in this paper are based on the total mass of MCS@MnO_2. MCS-MnO_2-outer anode underwent fast capacity decay from 1053 to 650 mAh g^{-1} within 50 cycles at a current density of 0.2 A g^{-1} and the final capacity approached that of pure MCSs (610 mAh g^{-1} at 50^{th} cycle, Figure S10), which likely suffers from the detachment of MnO_2 from carbon support due to the large volume change as illustrated in Scheme 1a. In contrast, MCS@MnO_2-5 exhibited a much better cycling behavior and no capacity fading was observed. After 50 cycles, a reversible capacity up to 970 mAh g^{-1} was retained. Considering the 40 wt% carbon in MCS@MnO_2-5, a capacity of 1210 mAh g^{-1} was contributed by the deposited MnO_2. This value is very close to its theoretical capacity of 1232 mAh g^{-1}, indicating complete utilization of MnO_2 active material in the electrochemical reaction. Even discharged/charged at high current densities of 1 and 2 A g^{-1}, MCS@MnO_2-5 electrodes delivered specific capacities of 803 and 710 mAh g^{-1}, respectively, after 200 deep cycles with 99% capacity retention (Figure 3d). The average CE of MCS@MnO_2-5 cycled at 1 and 2 A g^{-1} reached 99.2% (Figure S11), suggesting ultrahigh reversibility of the electrochemical reaction.

The rate capability of the MCS@MnO_2-5 anode was also tested at different current densities (Figure 3e). As the current density increased from 0.1 to 2 A g^{-1}, MCS@MnO_2-5 anode displayed reversible and stable capacities of 992 and 615 mAh g^{-1}, respectively. Even at a very high rate of 5 A g^{-1}, a stable capacity of 529 mAh g^{-1} can still be achieved. Particularly, when the current density switched back to the initial 0.1 A g^{-1}, the specific capacity completely recovered and remained stable in the subsequent cycles (Figure 3e). Moreover, the kinetic features of the charge/discharge curves at high current densities are similar to those at

low current densities (Figure S12), which highlights the excellent transport properties of both Li ions and electrons within the electrodes.

In order to further examine the effect of our hierarchical structure design on anodes with high active material loading, the electrochemical performance of MCS@MnO_2-24 with MnO_2 content as high as 90 wt% was investigated. Compared with MCS@MnO_2-5, MCS@MnO_2-24 showed a limited surface area of 30 m^2 g^{-1}, lower carbon content of 10% and a higher tap density (Figure S8), which can decrease the unwanted Li^+ consumption (SEI formation and Li^+ trapped in amorphous carbon) and contribute to high CE and volumetric capacity.[10b] When discharged/charged at low current density, there is one long plateau observed in the discharge curve of the MCS@MnO_2-24 and one plateau in the charge curve, implying that more MnO_2 is involved in the electrochemical reaction (Figure S13a-b). As expected, the initial CE of MCS@MnO_2-24 (78%) is apparently higher than 70% of MCS@MnO_2-5 and 48% of pure MCSs, confirming that less Li ions are consumed by the side reaction. During the cycling test at 1A g^{-1}, an activation process was also observed, which could be derived from the delayed wetting of electrolyte into the nanoporous hybrid electrode.[25] A high capacity of 850 mAh g^{-1} can be retained after 300 cycles (Figure 3f). Moreover, MCS@MnO_2-24 exhibited good rate capability; capacities at 0.1, 0.5, 2 and 5 A g^{-1} are 1104, 637, 354 and 186 mAh g^{-1} (Figure 3g and S13c), respectively. When the current density returned to 0.1 A g^{-1}, the specific capacity of MCS@MnO_2-24 also recovered and maintained around 1100 mAh g^{-1} in the subsequent cycles. The electrochemical performances of our MCS@MnO_2 anodes including initial CE, reversible capacity and cycling stability are superior to those of a wide range of MnO_x or MnO_x/C hybrid anodes reported in recent literature (Table S2).

The volumetric capacity is another critical concern for the implementation of novel anodes, largely dependent on the tap density of active materials. By calculating the real tap density of MCS@MnO_2-24 anodes, we estimated a volumetric capacity of 1200 mAh cm^{-3} at 0.1 A g^{-1}

(see Figure S14 for calculation details), which is nearly two times of 620 mAh cm^{-3} for the graphite anodes[17b] and even comparable to that of state-of-the-art nanostructured Si electrodes (Table S3). At the high current density of 1 A g^{-1}, a reversible volumetric capacity of 927 mAh cm^{-3} was reached after 300 deep cycles, which was around four times that (242 mAh cm^{-3})[26] of graphite anodes. These values can be further pushed forward by conventional processing optimization, such as pressing the electrodes under moderate pressure to get a compact electrode film with a higher packing density.[27]

To understand the superior electrochemical performance of MCS@MnO_2 electrodes, electrochemical impedance spectroscopy (EIS) measurements were carried out after the 1st and 200th cycle at a current density of 1 A g^{-1} (Figure S15). No obvious impedance increase was observed after 200 cycles, indicating the excellent stability of SEI and charge transfer process in the electrode. The morphology of hybrid electrodes after 200 cycles was examined by SEM (Figure S16). No cracks, pulverization or crumpling of the electrode materials were observed, and the products still maintained the spherical morphology, validating the excellent mechanical stability of MCS@MnO_2 anodes.

The high performance of our hierarchical MnO_2/C hybrid can be explained as follows: (1) the hollow core-shell MnO_2@C nanospheres in MCS@MnO_2 effectively solve the large volume variation and conductive problems of MnO_2 with well-developed inner voids and face-to-face contact mode, respectively, improving the mechanical stability of MCS@MnO_2 anodes; (2) The carbon framework as both an electrical speedway and mechanical skeleton boosts the utilization of MnO_2 in electrochemical reaction, leading to enhanced capacity of MCS@MnO_2; (3) The open porous structure of MCS@MnO_2 can further promote the electrolyte transport through the electrode by shortening the diffusion pathway, resulting in improved reaction kinetics for high rate capability.

In summary, hierarchically hollow core-shell MnO_2/C hybrid spheres were rationally constructed via a facile deposition process on the open porous MCSs. The loading of MnO_2

active material in the hybrid was readily controlled in the range of 50-90 wt%. Such hierarchical architecture provides a unique face-to-face contact mode between carbon frameworks and hollow MnO_2 nanospheres for robust electrical connection as well as well-developed inner voids for MnO_2 volume changes and fast ionic transport, simultaneously improving the mechanical stability, utilization and reaction kinetics of MnO_2 anodes. As a consequence, superior cycling performance and excellent rate capability were achieved for MCS@MnO_2 as the anode of LIBs. Such hierarchically hollow core-shell structure design can be further extended to other electrode materials for boosting up electrochemical energy storage and conversion applications.

Experimental Section

Experimental Details are included in the Supporting Information.

Supporting Information

Supporting Information is available from the Wiley Online Library or from the author.

Acknowledgements

This work was financially supported by the ERC grants for NANOGRAPH and 2DMATER, the EC under the Graphene Flagship (grant number CNECT-ICT-604391). The authors thank Dr. Ingo Lieberwirth, Gunnar Glasser and Katrin Kirchhoff for help with electron microscopy measurements.

Received: ((will be filled in by the editorial staff))
Revised: ((will be filled in by the editorial staff))
Published online: ((will be filled in by the editorial staff))

[1] a) M. Armand, J. M. Tarascon, *Nature* **2008**, *451*, 652; b) B. Dunn, H. Kamath, J.-M. Tarascon, *Science* **2011**, *334*, 928.

[2] M. T. McDowell, S. W. Lee, W. D. Nix, Y. Cui, *Adv. Mater.* **2013**, *25*, 4966.

[3] a) T. Kennedy, E. Mullane, H. Geaney, M. Osiak, C. O'Dwyer, K. M. Ryan, *Nano Lett.* **2014**, *14*, 716; b) K. H. Seng, M.-H. Park, Z. P. Guo, H. K. Liu, J. Cho, *Angew. Chem.* **2012**, *124*, 5755; *Angew. Chem. Int. Ed.* **2012**, *51*, 5657.

[4] X. Huang, S. Cui, J. Chang, P. B. Hallac, C. R. Fell, Y. Luo, B. Metz, J. Jiang, P. T. Hurley, J. Chen, *Angew. Chem.* **2015**, *127*, 1510; *Angew. Chem. Int. Ed. Engl.* **2015**, *54*, 1490.

[5] a) P. Poizot, S. Laruelle, S. Grugeon, L. Dupont, J. M. Tarascon, *Nature* **2000**, *407*, 496; b) M. V. Reddy, G. V. Subba Rao, B. V. R. Chowdari, *Chem. Rev.* **2013**, *113*, 5364.

[6] a) A. L. M. Reddy, M. M. Shaijumon, S. R. Gowda, P. M. Ajayan, *Nano Lett.* **2009**, *9*, 1002; b) H. Wang, L.-F. Cui, Y. Yang, H. Sanchez Casalongue, J. T. Robinson, Y. Liang, Y. Cui, H. Dai, *J. Am. Chem. Soc.* **2010**, *132*, 13978; c) H. Xia, M. Lai, L. Lu, *J. Mater. Chem.* **2010**, *20*, 6896; d) C. X. Guo, M. Wang, T. Chen, X. W. Lou, C. M. Li, *Adv. Energy Mater.* **2011**, *1*, 736; e) L. Li, C. Nan, J. Lu, Q. Peng, Y. Li, *Chem. Commun.* **2012**, *48*, 6945; f) L. Li, A.-R. O. Raji, J. M. Tour, *Adv. Mater.* **2013**, *25*, 6298.

[7] S. J. Ee, H. Pang, U. Mani, Q. Yan, S. L. Ting, P. Chen, *ChemPhysChem* **2014**, *15*, 2445.

[8] A. Yu, H. W. Park, A. Davies, D. C. Higgins, Z. Chen, X. Xiao, *J. Phys. Chem. Lett.* **2011**, *2*, 1855.

[9] M. Kundu, C. C. A. Ng, D. Y. Petrovykh, L. Liu, *Chem. Commun.* **2013**, *49*, 8459.

[10] a) N. Liu, H. Wu, M. T. McDowell, Y. Yao, C. Wang, Y. Cui, *Nano Lett.* **2012**, *12*, 3315; b) N. Liu, Z. Lu, J. Zhao, M. T. McDowell, H. W. Lee, W. Zhao, Y. Cui, *Nat Nanotechnol* **2014**, *9*, 187.

[11] H. Zhang, L. Zhou, O. Noonan, D. J. Martin, A. K. Whittaker, C. Yu, *Adv. Funct. Mater.* **2014**, *24*, 4337.

[12] Z. Cai, L. Xu, M. Yan, C. Han, L. He, K. M. Hercule, C. Niu, Z. Yuan, W. Xu, L. Qu, K. Zhao, L. Mai, *Nano Lett.* **2015**, *15*, 738.

[13] W. Zhou, Y. Yu, H. Chen, F. J. DiSalvo, H. D. Abruña, *J. Am. Chem. Soc.* **2013**, *135*, 16736.

[14] B. Wang, X. Li, X. Zhang, B. Luo, Y. Zhang, L. Zhi, *Adv. Mater.* **2013**, *25*, 3560.

[15] D. Chen, X. Mei, G. Ji, M. Lu, J. Xie, J. Lu, J. Y. Lee, *Angew. Chem.* **2012**, *124*, 2459; *Angew. Chem. Int. Ed.* **2012**, *51*, 2409.

[16] F. H. Du, B. Li, W. Fu, Y. J. Xiong, K. X. Wang, J. S. Chen, *Adv. Mater.* **2014**, *26*, 6145.

[17] a) A. Magasinski, P. Dixon, B. Hertzberg, A. Kvit, J. Ayala, G. Yushin, *Nat Mater* **2010**, *9*, 353; b) I. Kovalenko, B. Zdyrko, A. Magasinski, B. Hertzberg, Z. Milicev, R. Burtovyy, I. Luzinov, G. Yushin, *Science* **2011**, *334*, 75; c) R. Yi, F. Dai, M. L. Gordin, S. Chen, D. Wang, *Adv. Energy Mater.* **2013**, *3*, 295; d) B. Wang, X. Li, T. Qiu, B. Luo, J. Ning, J. Li, X. Zhang, M. Liang, L. Zhi, *Nano Lett.* **2013**, *13*, 5578.

[18] G. Wang, Y. Sun, D. Li, H.-W. Liang, R. Dong, X. Feng, K. Müllen, *Angew. Chem.* **2015**, *127*, 15406; *Angew. Chem. Int. Ed.* **2015**, *54*, 15191.

[19] a) J. Liu, S. Z. Qiao, H. Liu, J. Chen, A. Orpe, D. Zhao, G. Q. Lu, *Angew. Chem.* **2011**, *123*, 6069; *Angew. Chem. Int. Ed.* **2011**, *50*, 5947; b) S. Wang, W.-C. Li, G.-P. Hao, Y. Hao, Q. Sun, X.-Q. Zhang, A.-H. Lu, *J. Am. Chem. Soc.* **2011**, *133*, 15304; c) L.-F. Chen, Z.-H. Huang, H.-W. Liang, Q.-F. Guan, S.-H. Yu, *Adv. Mater.* **2013**, *25*, 4746.

[20] a) C. Liang, Z. Li, S. Dai, *Angew. Chem.* **2008**, *120*, 3754; *Angew. Chem. Int. Ed.* **2008**, *47*, 3696; b) Z. Jun, C. Jia-jia, Z. Cheng-long, Q. Hang, Z. Ming-sen, D. Quan-feng, *J. Mater. Chem. A* **2014**, *2*, 6343.

[21] a) Y. Deng, T. Yu, Y. Wan, Y. Shi, Y. Meng, D. Gu, L. Zhang, Y. Huang, C. Liu, X. Wu, D. Zhao, *J. Am. Chem. Soc.* **2007**, *129*, 1690; b) Y. Jiao, D. Han, L. Liu, L. Ji, G. Guo, J. Hu, D. Yang, A. Dong, *Angew. Chem.* **2015**, *127*, 5819; *Angew. Chem. Int. Ed. Engl.* **2015**, *54*, 5727.

[22] a) M. N. Patel, X. Wang, B. Wilson, D. A. Ferrer, S. Dai, K. J. Stevenson, K. P. Johnston, *J. Mater. Chem.* **2010**, *20*, 390; b) Z.-Y. Sui, C. Wang, K. Shu, Q.-S. Yang, Y. Ge, G. G. Wallace, B.-H. Han, *J. Mater. Chem. A* **2015**, *3*, 10403.

[23] a) S.-W. Lee, S.-M. Bak, C.-W. Lee, C. Jaye, D. A. Fischer, B.-K. Kim, X.-Q. Yang, K.-W. Nam, K.-B. Kim, *J. Phys. Chem. C* **2014**, *118*, 2834; b) J. Qian, H. Jin, B. Chen, M. Lin, W. Lu, W. M. Tang, W. Xiong, L. W. Chan, S. P. Lau, J. Yuan, *Angew. Chem.* **2015**, *127*, 6904; *Angew. Chem. Int. Ed. Engl.* **2015**, *54*, 6800.

[24] W. Wei, S. Yang, H. Zhou, I. Lieberwirth, X. Feng, K. Müllen, *Adv. Mater.* **2013**, *25*, 2909.

[25] H. Wu, G. Yu, L. Pan, N. Liu, M. T. McDowell, Z. Bao, Y. Cui, *Nat Commun* **2013**, *4*, 1943.

[26] Y. Xu, Z. Lin, X. Zhong, B. Papandrea, Y. Huang, X. Duan, *Angew. Chem.* **2015**, *127*, 5435; *Angew. Chem. Int. Ed. Engl.* **2015**, *54*, 5345.

[27] D. Lin, Z. Lu, P.-C. Hsu, H. R. Lee, N. Liu, J. Zhao, H. Wang, C. Liu, Y. Cui, *Energy Environ. Sci.* **2015**, *8*, 2371.

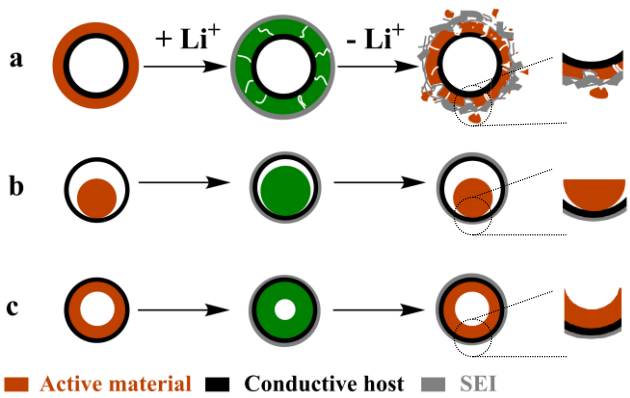

Scheme 1. Illustration of morphological changes of coating structure, yolk-shell and hollow core-shell structure during lithiation/delithiation process.

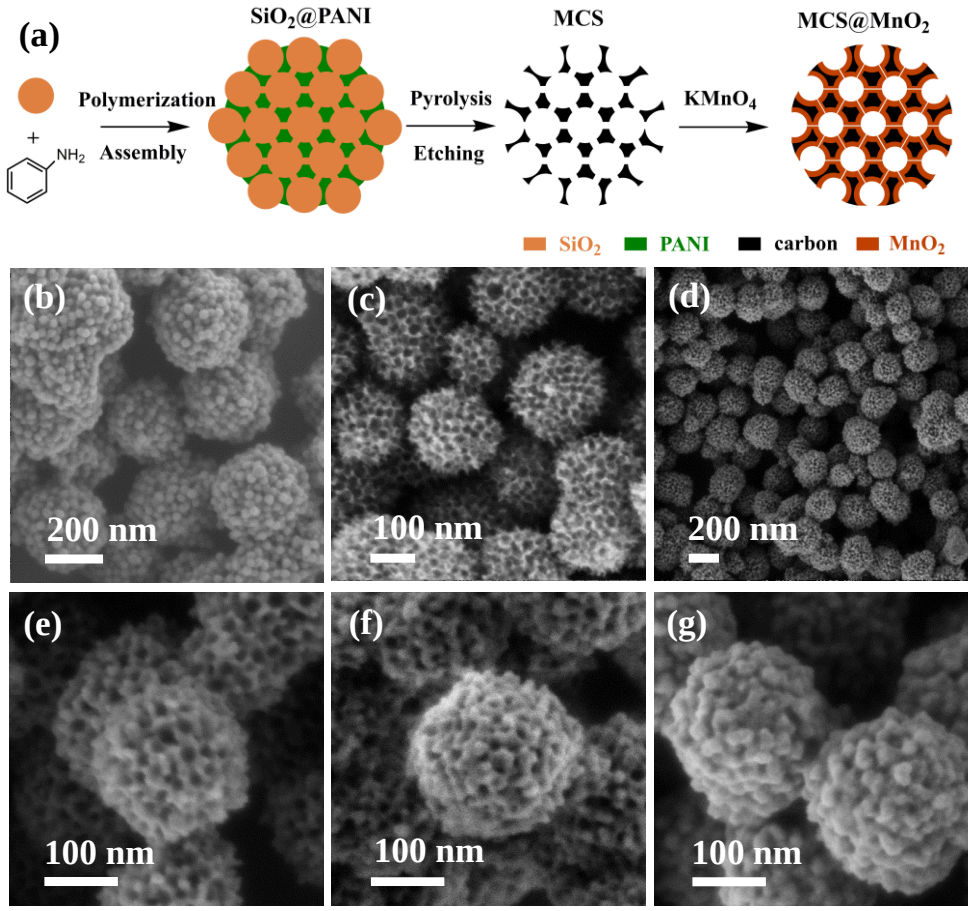

Figure 1. (a) The formation process of MCS@MnO_2 spheres. SEM images of (b) SiO_2@PANI, (c) MCSs, (d, e) MCS@MnO_2-2, (f) -5 and (g) -24.

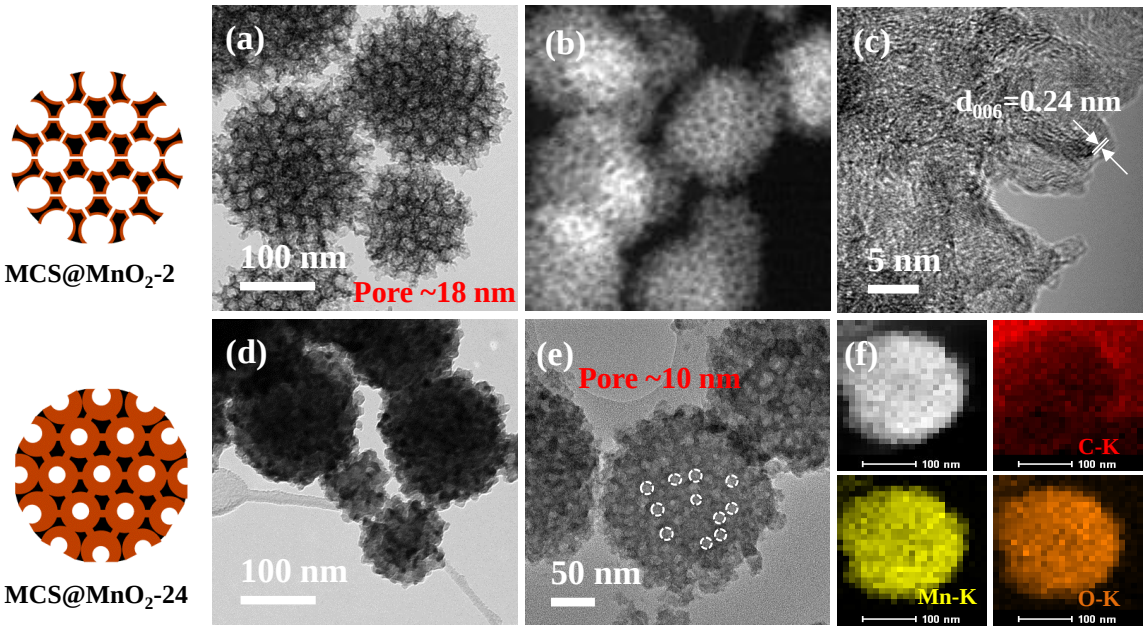

Figure 2. (a, b) Bright and dark-field TEM and (c) HRTEM images of MCS@MnO_2-2. TEM images of (d) MCS@MnO_2-24 and (e) its ultrathin slice. (f) TEM-EDS elemental mapping images of the resultant MCS@MnO_2-24 slice.

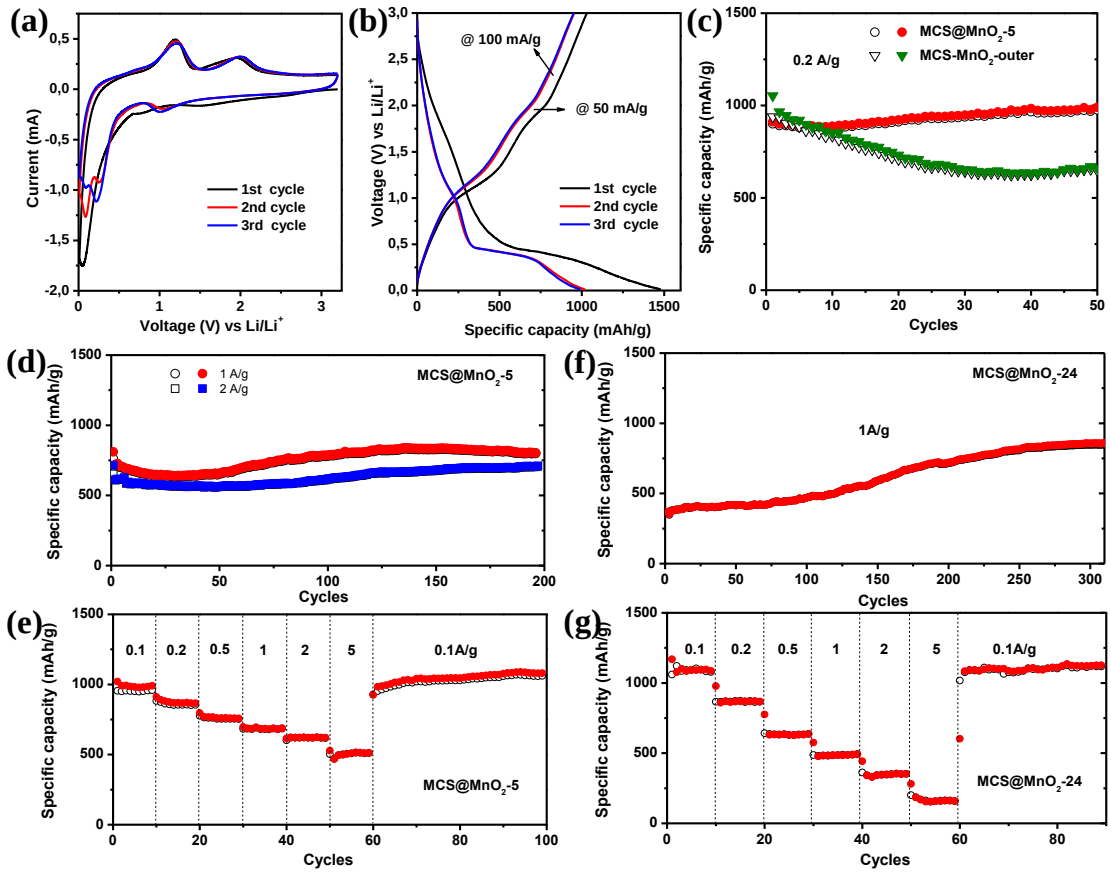

Figure 3. Electrochemical properties of MCS@MnO_2. (a) Cyclic voltammetry, (b) initial three charge-discharge curves and (c) cycling performance of different samples at 0.2 A/g. (d, f) Cycling performance and (e, g) rate capability of MCS@MnO_2-5 and -24.

Hierarchical MnO_2/C hybrid spheres (MCS@MnO_2), consisting of numerous hollow core-shell MnO_2@C nanospheres, are developed via a facile deposition process. The well-defined inner voids and robust carbon framework endow MCS@MnO_2 with excellent mechanical stability, efficient utilization of MnO_2 and enhanced reaction kinetics for Li-ion batteries, therefore leading to large specific capacities, superior rate capability and long-term cycling stability.

Keyword: hierarchical structures, hollow core-shell, mesoporous MnO_2, hybrids, Li-ion batteries

Gang Wang, Yuhan Sun, Debao Li, Wei Wei, Xinliang Feng* and Klaus Müllen*

Constructing Hierarchically Hollow Core-Shell MnO_2/C Hybrid Spheres for High-Performance Lithium Storage